Supporting Information:

Fast Increase of Nanofluidic Slip in Supercooled Water: the Key Role of Dynamics

Cecilia Herrero,[†] Gabriele Tocci,[‡] Samy Merabia,[†] and Laurent Joly[*,†]

†*Univ Lyon, Univ Claude Bernard Lyon 1, CNRS, Institut Lumière Matière, F-69622, VILLEURBANNE, France*

‡*Department of Chemistry, Universität Zürich, 8057 Zürich, Switzerland*

¶*Institut Universitaire de France (IUF)*

E-mail: laurent.joly@univ-lyon1.fr

MD Simulations Details

All the simulations were carried out with the LAMMPS package.[S1] The confined system consisted in a fluid (water or methanol) between two parallel walls (Fig. S1), with periodic boundary conditions applied in the directions parallel to the walls. For water simulations, 4096 water molecules were modeled with the TIP4P/2005 force field.[S2] Two different kinds of walls were considered. First, we modeled wall atoms which interact via a Lennard-Jones (LJ) potential. The interaction parameters between LJ walls and water molecules were set from[S3] for hydrophobic walls corresponding, for TIP4P/2005 at $300\,\mathrm{K}$, to a contact angle $\theta \sim 134°$ (computed through the sessile droplet method, following a procedure described in Ref. S4). The structure of the walls consisted in a frozen face centered cubic crystal constituted by three atomic layers exhibiting a (001) face to the fluid, with a lattice parameter $a = 5.356\text{Å}$

(Fig. S1). Second, we also simulated graphene walls with cross-interaction parameters taken from Ref. S5, characterized by a contact angle $\theta \sim 80°$ for TIP4P/2005 water at 300 K.
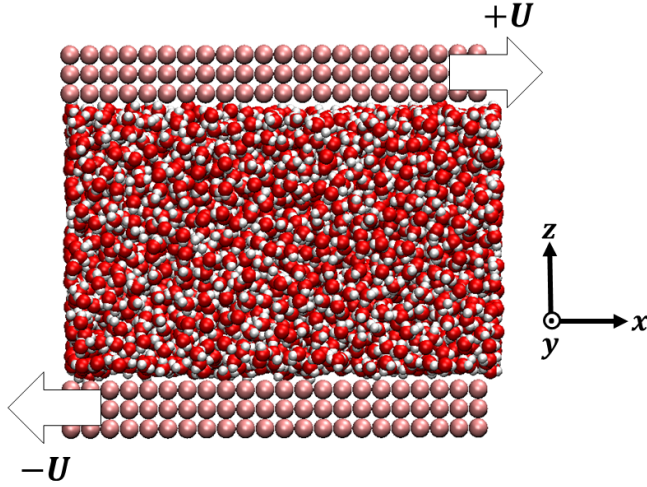

Figure S1: Modeled system constituted by a confined fluid between two planar solid walls. The snapshot corresponds to TIP4P/2005 water enclosed by LJ walls. The arrows indicate the shear velocity U directions by which the system is driven out of equilibrium for the shear flow measurements.

For methanol (MeOH) simulations, 4056 molecules were modeled with the interaction parameters given by Ref. S6,S7. For LJ walls and graphene we considered the same interactions between atoms than the ones for water and the cross interactions MeOH-wall were determined via Lorentz-Berthelot mixing rules. The surfaces were then characterized for MeOH at 300 K by contact angles $\theta \sim 100°$ and $\theta \sim 0°$ for LJ and graphene walls respectively. The wall dimensions were $L_x = L_y = 58.92$Å for the LJ wall, and $L_x = 56.57$Å, $L_y = 58.92$Å for graphene. The pressure was set to 1 atm by using the top wall as a piston during a preliminary run. The vertical height was then obtained by fixing the top wall at its equilibrium position for the given pressure and it corresponded to $H \sim 40$Å for water and $H \sim 90$Å for MeOH. We carried out an additional test, which consisted of 4 independent calculations of water confined between Lennard-Jones walls at a given temperature of 300 K and a given shear velocity of 10^{-4} Å/fs, leaving the top wall free to move around its equilibrium position. Here, we compare these set of results to those reported in the main text. The viscosity, friction coefficient and slip-length computed with freely moving walls, with an

average height of the confined fluid $H_{\text{top−free}} = 40.4$ Å, were:

$$\eta_{\text{top−free}} = 7.21 \times 10^{-4} \pm 4.41 \times 10^{-5} \text{ Pa} \cdot \text{s},$$

$$\lambda_{\text{top−free}} = 2.25 \times 10^{5} \pm 3.62 \times 10^{4} \text{ Pa} \cdot \text{s/m},$$

$$b_{\text{top−free}} = 32.3 \pm 6.80 \text{ Å};$$

whereas with a fixed height of $H_{\text{top−fixed}} = 40.2$ Å we obtained:

$$\eta_{\text{top−fixed}} = 8.10 \times 10^{-4} \pm 8.47 \times 10^{-5} \text{ Pa} \cdot \text{s},$$

$$\lambda_{\text{top−fixed}} = 2.22 \times 10^{5} \pm 1.17 \times 10^{4} \text{ Pa} \cdot \text{s/m},$$

$$b_{\text{top−fixed}} = 36.72 \pm 5.81 \text{ Å};$$

concluding that both procedures are equivalent, providing the same results within the error bars.

The temperature T was varied between 225 and 360K, by applying a Nosé-Hoover thermostat to the liquid (only along the directions perpendicular to the flow for non-equilibrium simulations). Equivalent results were obtained for different damping times, and with a Berendsen thermostat.

To measure the hydrodynamic transport coefficients we performed non-equilibrium molecular dynamics (NEMD) simulations applying a constant shear velocity U to the walls in opposite x directions for each wall (see Fig. S1), producing a Couette (linear) velocity profile far from the wall. The viscosity was measured from the ratio between the shear stress and the bulk shear rate, $\eta = \tau / \partial_z v_x$, where v_x corresponds to the velocity profile in the bulk region in the direction of the flow. The friction coefficient λ was measured from the ratio between the shear stress τ and the velocity jump at the interface $\Delta v = U - v_x(z_s)$, where v_x is the fitted bulk velocity profile in the direction of the flow evaluated at the effective wall position z_s. This effective wall position can be rationalized in terms of a Gibbs dividing

plane (GdP) which corresponds to a partitioning of space between a region of homogeneous liquid and vacuum (which would correspond to the wall region).[S8] This GdP will define an effective boundary condition at z_s at a distance Δ of the physical wall position. Considering the physical distance between walls as H then the hydrodynamic height h will be given by the relation $h = H - 2\Delta$. For a generic liquid, h is defined in terms of the GdP and it can be expressed as $h = N/(n_{\text{bulk}}S)$, where N is the total number of liquid particles, n_{bulk} bulk number density and S the walls surface. The extension of this formula for a molecular liquid is:

$$h = \frac{M}{\rho_{\text{bulk}}S},\tag{1}$$

where now M is the total liquid mass and ρ_{bulk} its bulk mass density. Because Eq. (1) relates the hydrodynamic height to static density profiles quantities, the density bulk mass density was computed from EMD simulations, computationally less expensive than the NEMD ones.

Both interfacial and bulk equations can be combined in the so-called "partial slip boundary condition",[S9]

$$\Delta v = \frac{\eta}{\lambda}\partial_z v_x\bigg|_{z=z_s} = b\partial_z v_x\bigg|_{z=z_s},\tag{2}$$

where the slip length b was measured from the relation $b = \eta/\lambda$.

Results

VTF, SA, Bässler laws: Theory

Viscosity temperature dependence is well described for liquids with strong intra-molecular bonds by an Arrhenius law,

$$\eta = \eta_0 \cdot \exp\left(\frac{A}{T}\right),\tag{3}$$

with activation energy $A > 0$. Nevertheless, fragile liquids, such as water, are characterized by a faster increase. Several models are proposed in the literature.[S10] Denoting the transport

coefficient as X, the most accepted ones are the Vogel-Tammann-Fulcher (VTF) law,[S11–S13] the Speedy-Angell (SA) law,[S14] and the Bässler (B) law,[S15] respectively:

$$X = X_0 \cdot \exp\left(\frac{A}{T - T_f}\right), \tag{4a}$$

$$X = X_0 \cdot \left(\frac{T}{T_f} - 1\right)^{-\gamma}, \tag{4b}$$

$$X = X_0 \cdot \exp\left(\left(\frac{T}{T_f}\right)^2\right). \tag{4c}$$

All these laws introduce a singularity at a finite temperature $T_f > 0$ so their applicability is restricted to temperatures away from this singularity. Specifically for water, while the above laws provide a good effective description of the temperature evolution of dynamical quantities down to deep supercooling (see below), they fail to describe the extreme supercooled region, where a dynamical cross-over between a fragile and a strong behavior appears, which can be captured by the two-state models of water.[S16] Accordingly, T_f does not provide a good indication of the true glass temperature transition of water.

VTF, SA, Bässler laws: Application to viscosity

We first computed the shear viscosity η from NEMD with LJ walls to assess the applicability of the different temperature dependence laws to our simulation results, Eq. (3) and Eq. (4), as done by previous experimental and numerical works.[S7,S17–S20] For TIP4P/2005 water we find good agreement between our data and a previous numerical work,[S20] as shown in Fig. S2. The fit results are reported in Table S1.

Due to the good agreement of VTF and SA fits with our numerical data (Fig. S3) we performed χ^2 and R^2 tests to determine which one describes better the results. We obtained $\{\chi^2, R^2\} = \{8.47 \cdot 10^{-5}, 0.9994\}$ for VTF and $\{\chi^2, R^2\} = \{3.87 \cdot 10^{-4}, 0.9956\}$ for SA therefore concluding a better agreement with VTF.

For MeOH simulations viscosity temperature dependence is less strong than for water
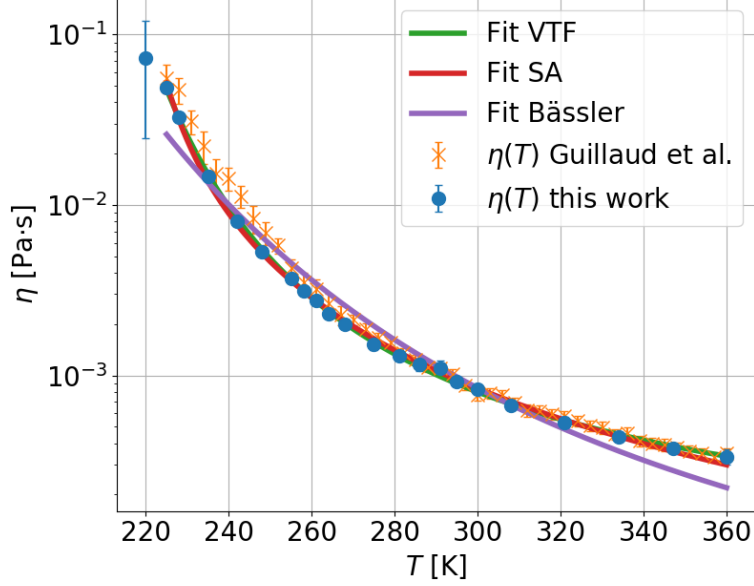
Figure S2: Shear viscosity NEMD measurements for TIP4P/2005 water. Our data set is in good agreement with previous work performed for the TIP4P/2005f force field.[S20] Three different fits, VTF, SA and Bässler were performed.

Table S1: Fit parameters of VTF Eq. (4a) and Arrhenius Eq. (3) laws for TIP4P/2005 water and MeOH respectively. We appreciate the similarity of the temperature T_f and the activation energy A between the different transport coefficients, η and λ, and between the two different wall types, LJ walls and graphene. X_0 units are [Pa s] for viscosity and [Pa s/m] for friction.

	TIP4P/2005 - VTF		
	T_f (K)	A (K)	X_0
η	176.26 ± 1.35	329.10 ± 11.43	$5.60 \cdot 10^{-5} \pm 3.72 \cdot 10^{-6}$
λ_{LJ}	165.94 ± 2.68	357.20 ± 20.99	$1.59 \cdot 10^{4} \pm 1.70 \cdot 10^{3}$
$\lambda_{\mathrm{graphene}}$	153.80 ± 4.16	349.32 ± 27.33	$1.60 \cdot 10^{3} \pm 1.93 \cdot 10^{2}$
	MeOH - Arrhenius		
	A (K)	X_0	
η	1357.35 ± 22.25	$5.22 \cdot 10^{-6} \pm 4.20 \cdot 10^{-7}$	
λ_{LJ}	1056.72 ± 35.63	$8.11 \cdot 10^{3} \pm 1.05 \cdot 10^{3}$	
$\lambda_{\mathrm{graphene}}$	899.31 ± 36.71	$3.43 \cdot 10^{2} \pm 4.56 \cdot 10^{2}$	

(Fig. S4). The results are in good agreement with previous work[S7] and well described by an Arrhenius law (Table S1).
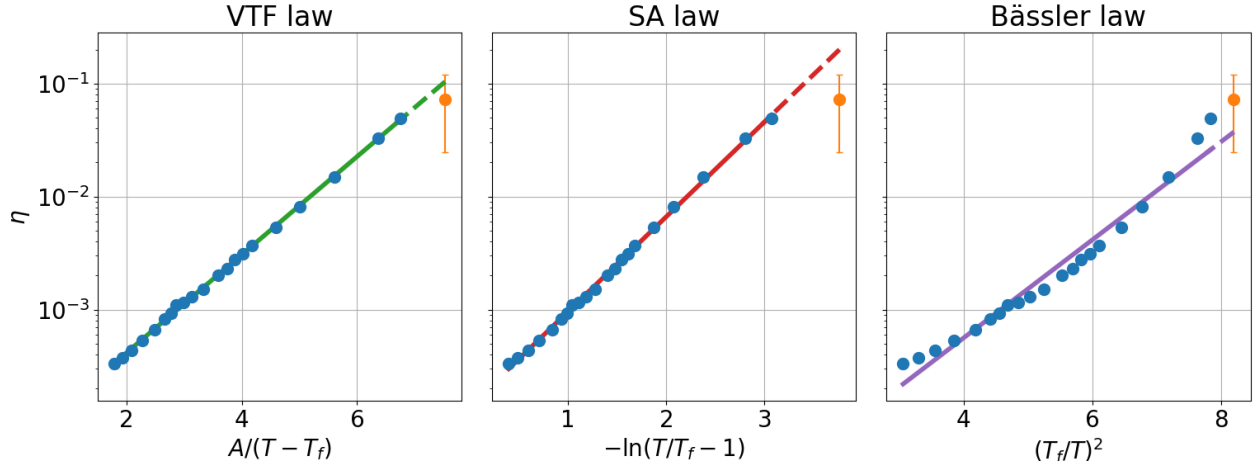
Figure S3: Different fits comparison for water shear viscosity. One can observe that our results are globally well described by VTF and SA laws but not by Bässler law. In orange the measure corresponding to $T = 220\,\mathrm{K}$, not taken into account for the fit due to its bigger error. Nevertheless when extending the fit results to lower temperatures this point is well described by VTF law but not by SA law, indicating the better suitability of VTF law for our data, in agreement with the results of the χ^2 and R^2 tests performed.
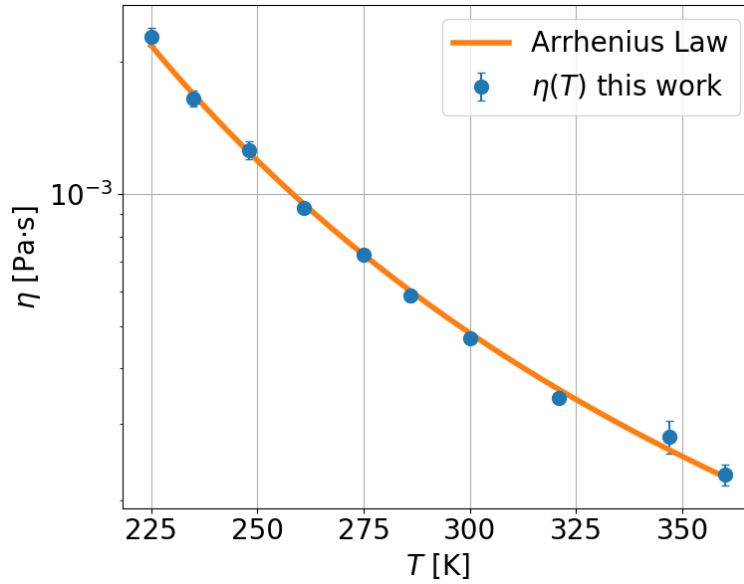

Figure S4: Shear viscosity NEMD measurements for MeOH. An Arrhenius fit was performed to our data set in order to describe viscosity temperature dependence.

VTF, SA, Bässler laws: Application to friction

For a given fluid, when varying the wall type we already see a difference in the absolute value of λ being more than one order of magnitude bigger for LJ walls than for graphene (Figs. S5,S8). This effect has already been appreciated and discussed in previous work[S5,S21]

and it is due to graphene extreme smoothness, which makes the liquid-solid friction extremely small ($\lambda \sim 1.7 \cdot 10^4$ Pa·s/m for water at 300K). The temperature dependence of friction can be fitted by the same laws than viscosity (Figs. S6,S7). Indeed, in Table S1 we can see that the law that better describes λ temperature dependence is in good agreement with the law that describes the viscosity (VTF for water and Arrhenius for MeOH). However, although very similar, the fit parameters for viscosity and friction are different beyond the error bars.
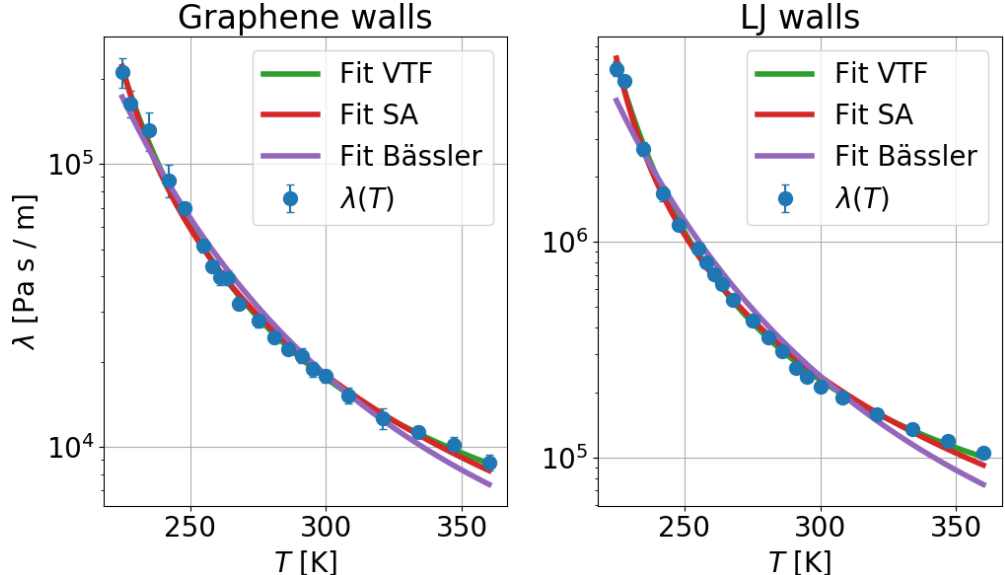

Figure S5: Liquid-solid friction coefficient results for TIP4P/2005 water from NEMD simulations for graphene and LJ walls respectively. Although the temperature evolution is similar for both walls, we can appreciate a one order of magnitude difference at a given temperature between the different walls. Three different fits, VTF, SA and Bässler were performed.

Discussion on Eq. (3) of the main text

In[S22] Bocquet and Barrat proposed a decomposition of the friction coefficient in different static and dynamical quantities:

$$\lambda \simeq \frac{S(q_\parallel)}{2D(q_\parallel)k_B T} \int_0^\infty \mathrm{d}z \rho(z) V_{\mathrm{FS}}^2(z), \tag{5}$$

where $S(q_\parallel)$ is the 2D structure factor in the contact layer, evaluated at the shortest wave vector of the solid surface $q_\parallel$, $\rho(z)$ is the fluid number density, V_{FS} the amplitude of the
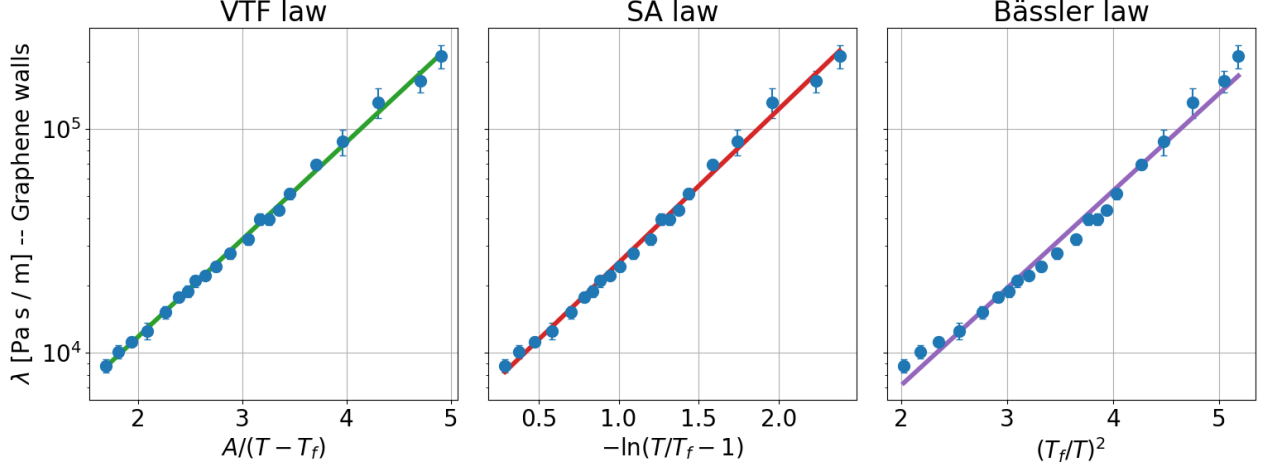
Figure S6: Different fits comparison for water-graphene friction coefficient. We can observe that, as in the case of bulk water's viscosity, our results are globally well described by VTF and SA laws but not by Bässler law.
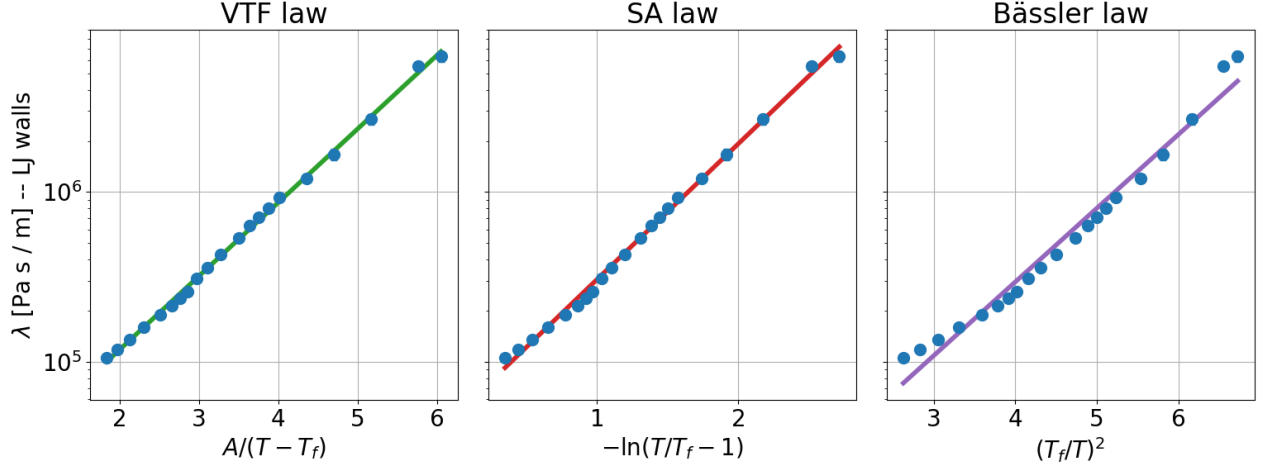

Figure S7: Different fits comparison for water-LJ walls friction coefficient. We can observe that, as in the case of bulk water's viscosity, our results are globally well described by VTF and SA laws but not by Bässler law.

first mode of the Fourier decomposition of the fluid-solid potential energy, and $D(q_\parallel)$ is the collective diffusion coefficient. $D(q_\parallel)$ can be expressed as $D(q_\parallel) = 1/(q_\parallel^2 \tau_\rho)$, where τ_ρ is the relaxation time of the intermediate scattering function $F(q_\parallel, t)$,

$$\tau_\rho = \int_0^\infty \mathrm{d}t F(q, t) = \int_0^\infty \mathrm{d}t \frac{\langle \rho_{q_\parallel}(t) \rho_{-q_\parallel}(0) \rangle}{\langle \rho_{q_\parallel}(0) \rho_{-q_\parallel}(0) \rangle}. \tag{6}$$
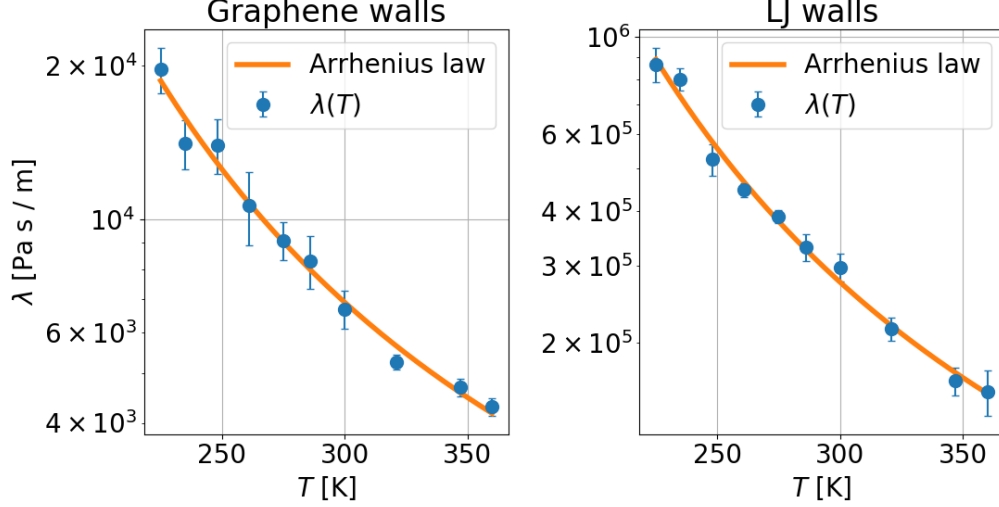
Figure S8: Liquid-solid friction coefficient results for MeOH for graphene and LJ walls respectively. Although the temperature evolution is similar for both walls, we can appreciate a much lower friction coefficient for graphene. An Arrhenius fit was performed.

We can then rewrite Eq. (5) in terms of τ_ρ and the force corrugation $f_{q_\parallel} = q_\parallel V_{\text{FS}}$ as:

$$\lambda \equiv \lambda_{\text{STAT}} \cdot \lambda_{\text{DYN}}, \quad \text{with} \quad \lambda_{\text{STAT}} \approx S(q_\parallel) \int_0^\infty \mathrm{d}z \, \rho(z) f_{q_\parallel}^2(z), \quad \text{and} \quad \lambda_{\text{DYN}} \approx \frac{\tau_\rho}{2 k_B T}. \quad (7)$$

It is interesting to note that in Bocquet and Barrat's paper, for a LJ fluid, only one single decay time for the density autocorrelation is considered, i.e. $\tau_\rho \equiv \tau_\alpha$, while in the case of water it is of great importance for a full description to consider the total decay time, obtained as the weighted sum of the two different decay times of $F(q, t)$, i.e. $\tau_\rho = (1 - A)\tau_\beta + A\tau_\alpha$.[S23]

We tested the qualitative validity of Eq. (7) by plotting the ratio $\lambda/(\lambda_{\text{STAT}} \cdot \lambda_{\text{DYN}})$. In Fig. S9 we can observe that for graphene and LJ walls this ratio remains constant with temperature, verifying the suitability of Eq. (7) as a qualitative decomposition of friction static and dynamic contributions temperature dependence.

Temperature dependence of the static structure factor

With regard to the T dependence of the static structure factor $S(q)$, one can observe for bulk in Fig. S10 the growth of a secondary peak for low wave vectors q when the temperature is
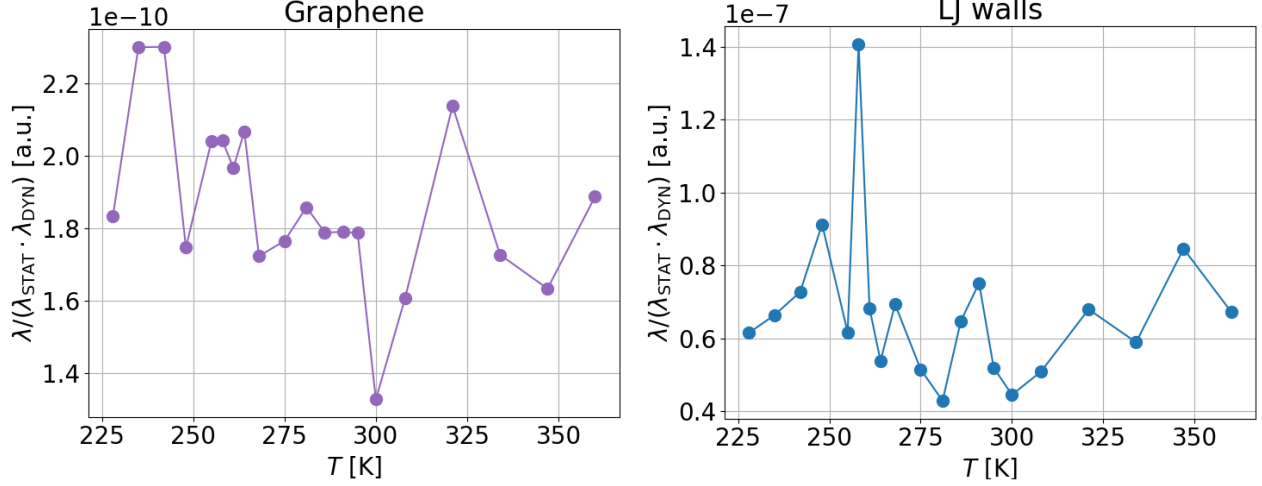
Figure S9: Ratio between the friction coefficient λ measured from NEMD simulations and the theoretical decomposition in static λ_{STAT} and dynamic λ_{DYN} contributions from Eq. (7). We can observe that the ratio remains constant with temperature, meaning a correct qualitative description of λ temperature dependence by Eq. (7).

lowered. One also sees a small dependence on temperature of the maximum of $S(q)$, located around $3\,\text{Å}^{-1}$. With regard to the interface, one can also see in Fig. S11 a small temperature dependence of the maximum of $S(q)$, located in a similar wave vector for both interface and close to the bulk value. Nevertheless, for the interface it is not the $S(q)$ value corresponding to the maximum that should be taken into account to study friction temperature dependence, but the one corresponding to the wall lattice vector, $q_{\parallel}$, with $q_{\parallel} = 1.66\,\text{Å}^{-1}$ for LJ walls and $q_{\parallel} = 2.55\,\text{Å}^{-1}$ for graphene, both surface wave vectors being represented with dotted black line in Fig. S11, where we can see that we can consider them constant with temperature.

Calculation of the static contribution to friction

For graphene walls, we took the values for $f_{q_{\parallel}}$ from Falk et al.,[S5] whose results are well described by a fit, in arbitrary units, of the form $f_{q_{\parallel}} = B \exp(-Az)$, with $B = \exp(14.79)$ and $A = 5.33\,\text{Å}^{-1}$. For LJ wall, an analytical expression for the force corrugation was derived by Steele.[S24] In this case,

$$f_{q_{\parallel}} = \frac{4\pi}{d_{\mathrm{LJ}}}\varepsilon_{\mathrm{LJ}}E_1(z),\tag{8}$$
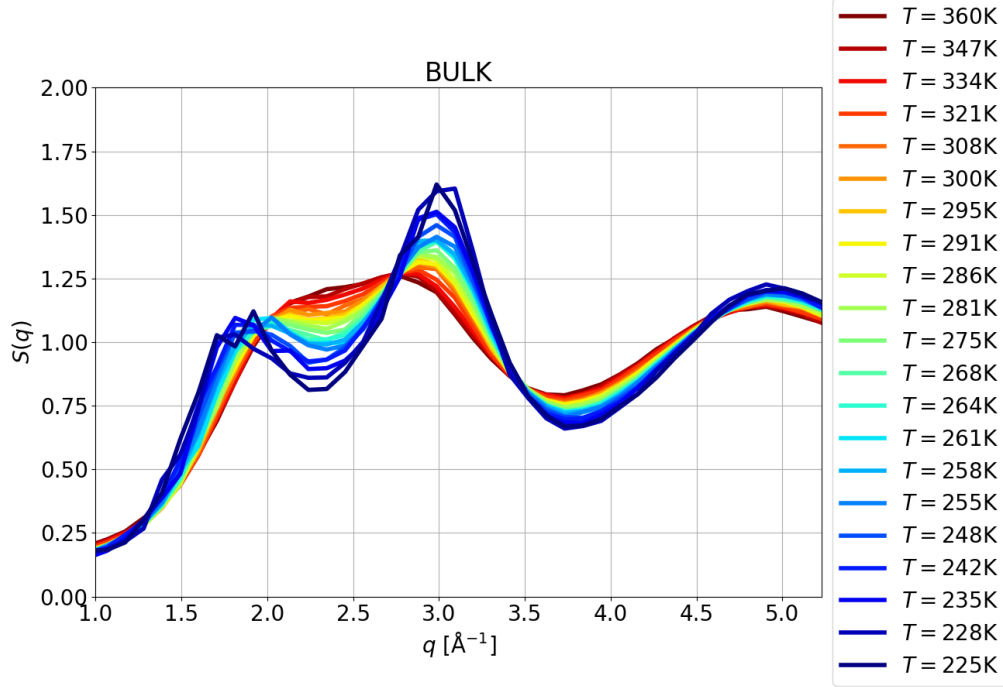
Figure S10: Temperature evolution of the static structure factor of bulk water. One can observe a small temperature dependence of the maximum of $S(q)$ located at $q \sim 3\,\mathring{A}^{-1}$ as well as the appearance of a secondary peak at a lower wave vector q when lowering the temperature.
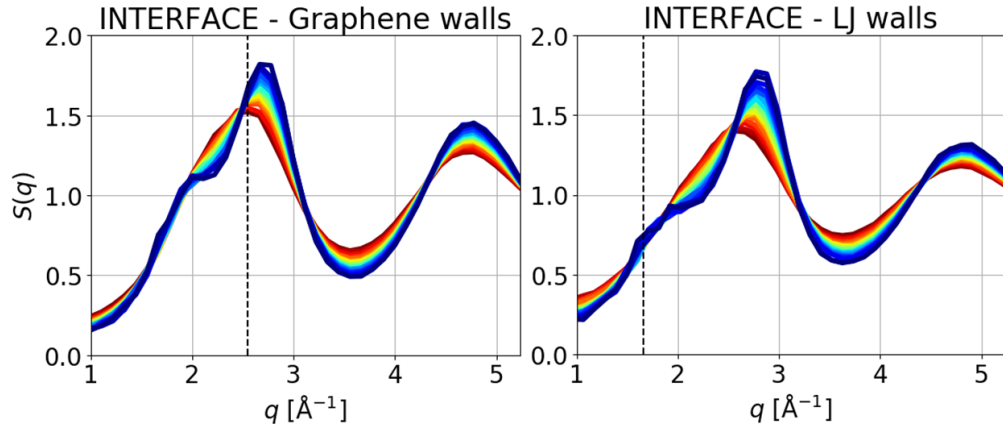

Figure S11: Temperature evolution of static structure factor for water on graphene and LJ walls, computed in the interfacial region, defined as the liquid region between the wall and the first minimum of the liquid density profile. Black dashed line corresponds to the shortest wave vector of the solid surface, $q_{\parallel}$. We can observe that $S(q_{\parallel})$ remains constant with temperature. The temperature coloring scheme is the same as in Fig. S10.

where

$$E_1(z) = 2\pi A^6 \left[\frac{A^6}{30} \left(\frac{\pi d_{\mathrm{LJ}}}{z} \right)^5 K_5 \left(\frac{2\pi z}{d_{\mathrm{LJ}}} \right) - 2 \left(\frac{\pi d_{\mathrm{LJ}}}{z} \right)^2 K_2 \left(\frac{2\pi z}{d_{\mathrm{LJ}}} \right) \right], \tag{9}$$

with K_n being to the modified Bessel function of the second kind, $\varepsilon_{\mathrm{LS}}$ and σ_{LS} the LJ interaction energy and size between liquid and solid atoms, d_{LJ} the equilibrium distance between solid atoms and $A = \sigma_{\mathrm{LS}}/d_{\mathrm{LJ}}$. The force corrugation is represented as a function of distance in Fig. S12 for both walls.
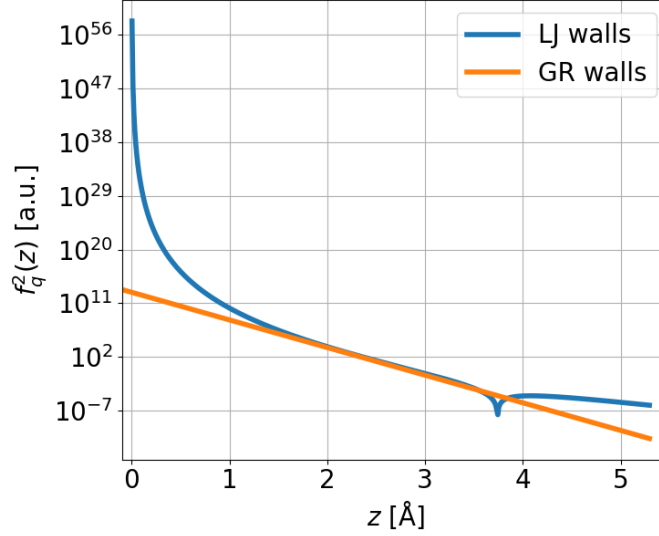

Figure S12: Squared force corrugation f_q^2, in arbitrary units, as a function of the distance from the wall for LJ walls and graphene. We can observe a strong decay with increasing z.

The other structural parameter needed to compute the integral in Eq. (7) is the number density profile. Its evolution with temperature can be found in Figs. S14,S13, where one can observe a noisy region of the density profile close to the wall in the case of LJ walls. In Fig. S15, representing the density multiplied by the force corrugation squared, one can observe that this noise becomes significant for the highest temperatures when it is multiplied by $f_{q_{\parallel}}^2$, which strongly increases when getting closer to the wall. In order to decrease such noise, we considered a density behavior close to the wall as $n_{\mathrm{dens}} = A \exp(-B/z^n)$ and fitted this function for the LJ walls, obtaining $n \sim 2.5$. We can appreciate in continuum line in Fig S15 the results considering the fitted density profile. In Fig. S16 right we can compare the original data with the fitted results integrals. We see that the main difference between both data sets are for the two highest temperatures (the noisiest ones, $T = \{347, 360\}$ K) while the fitting procedure accurately describes the rest of the results. In Fig. S16 we can

observe, for both walls, two different temperature behaviors of the static integral. For the higher temperatures it behaves as a power law of the form $b\,x^a$, with $a \sim 0.5$ for graphene and $a \sim 3$ for LJ walls, while for the lower temperatures the integral remains constant with temperature.
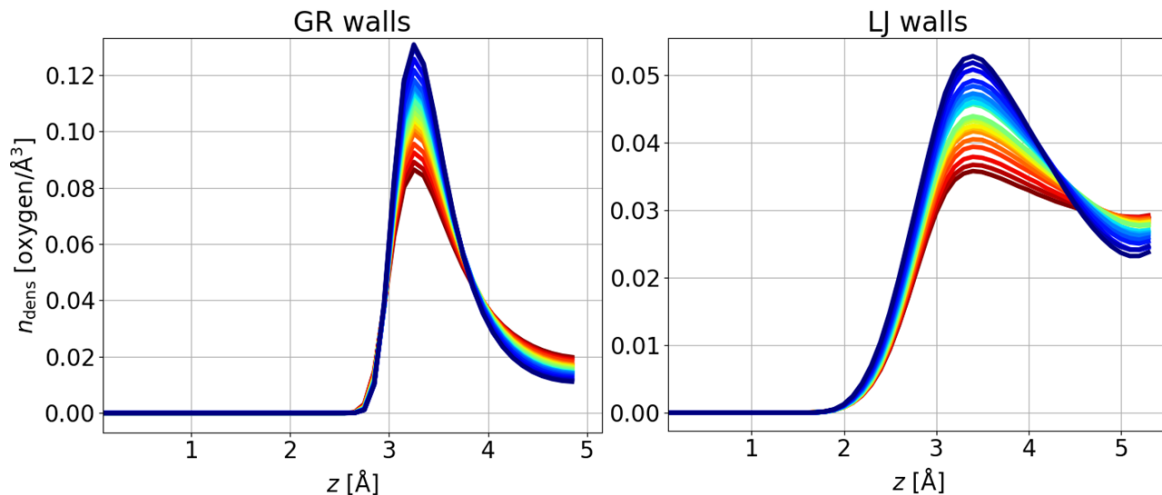

Figure S13: Oxygen number density profiles for water-graphene and water-LJ walls respectively with the surface wall atoms located at $z = 0\,\mathring{A}$. The temperature coloring scheme is the same as in Fig. S10.
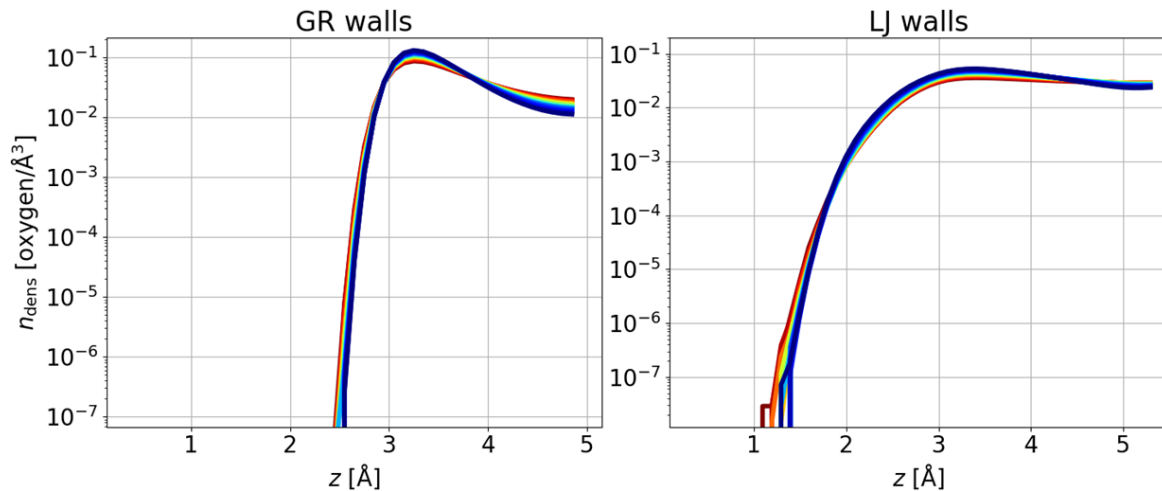

Figure S14: Oxygen number density profiles for water-graphene and water-LJ walls respectively with the surface wall atoms located at $z = 0\,\mathring{A}$, with a log scale for the density. The temperature coloring scheme is the same as in Fig. S10.
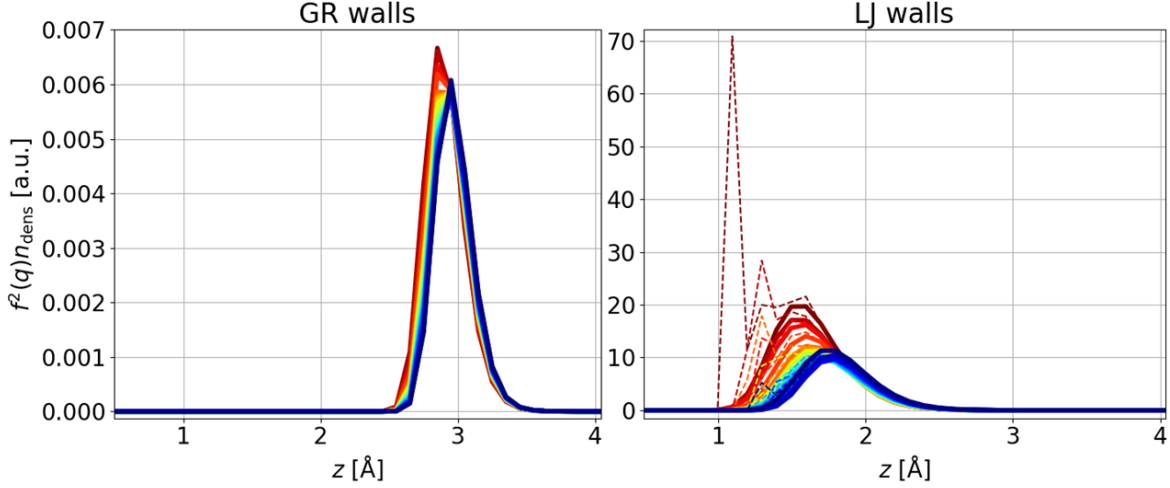
Figure S15: Product of oxygen number density n_{dens} and the squared force corrugation f_q^2, in arbitrary units, as a function of the wall distance whose surface is located at $z = 0\,\mathring{A}$, for graphene and LJ walls respectively. For LJ walls, the original data are represented in dashed lines, and we can observe a noisy region at short distances for the highest temperatures. In continuum line are represented the results of fitting the density at short distances as $n_{\mathrm{dens}} = A\exp(-B/z^n)$ in order to remove the noise. No fit was needed for graphene walls, and the original data are represented in continuum line.
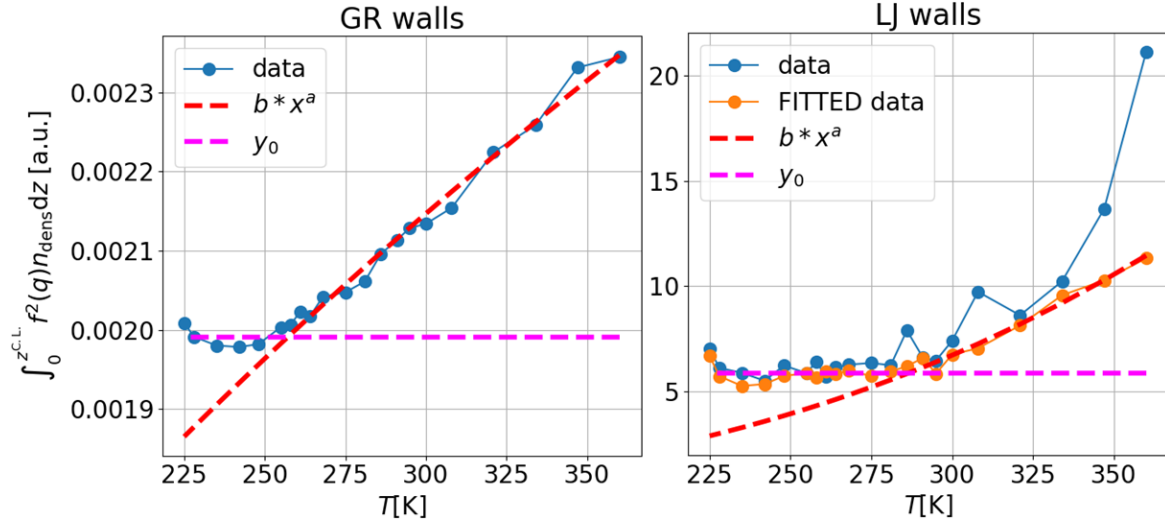

Figure S16: Static part integral from Eq. (7) as a function of temperature for water-graphene and water-LJ walls respectively. For LJ walls the original and the fitted density data are plotted. We can observe that the fit is in agreement with the data except for the two highest temperatures, $T = \{347, 360\}$ K. In dashed lines are represented the fits for the two different temperature behaviors observed for both walls: a power law for high temperatures and a constant value for the lower ones.

Characteristic times

Fig. S17 shows the results for the different characteristic times for bulk and interface obtained from the fit of the intermediate scattering function $F(q, t)$. We can observe that the long relaxation time τ_α increases fast when decreasing temperature, while the short relaxation time τ_β remains constant. In this figure one can observe a small but systematic difference between bulk and interfaces for τ_β as well. The VTF fit results for the total relaxation time τ_ρ are shown in Table S2.
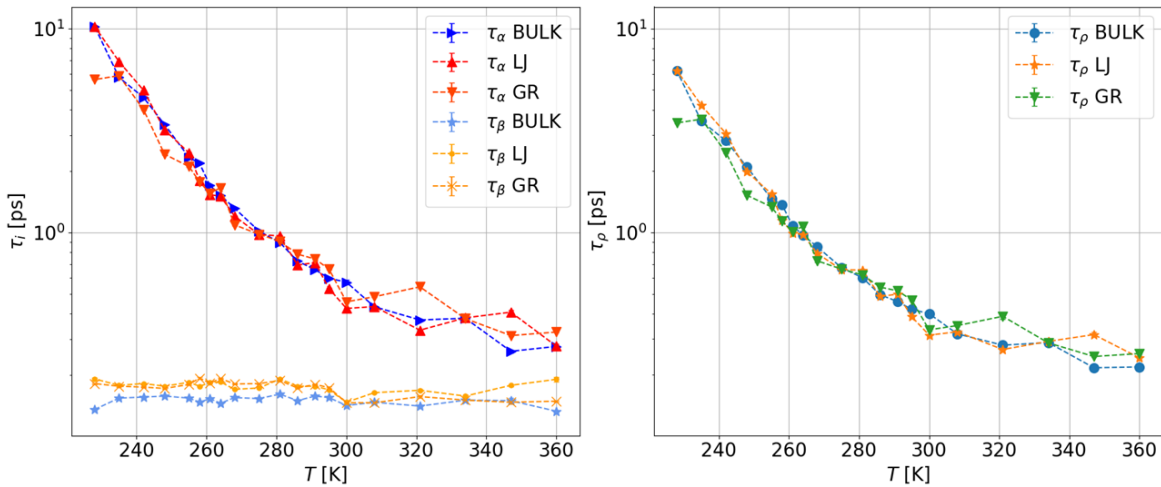

Figure S17: Characteristic times τ_α, τ_β and τ_ρ as a function of temperature for bulk water, water-LJ wall and water-graphene interfaces. We can observe that the main dynamic contribution for the transport properties temperature evolution comes from τ_α, while τ_β remains constant with temperature. A small but systematic difference between bulk and interface is found for τ_β. Nevertheless, because the main contribution at low temperatures to the total relaxation time is τ_α, τ_ρ is similar for bulk and the different surfaces.

Table S2: Fit parameters of VTF Eq. (4a) law for the total relaxation time τ_ρ for TIP4P/2005 bulk water and confined between the two different wall types, LJ walls and graphene.

	TIP4P/2005 - VTF		
	T_f (K)	A (K)	X_0 (ps)
τ_ρ bulk	165.69 ± 6.18	322.34 ± 41.23	$3.70 \cdot 10^{-2} \pm 7.43 \cdot 10^{-3}$
τ_ρ LJ walls	144.76 ± 22.49	578.63 ± 213.33	$2.06 \cdot 10^{-2} \pm 1.72 \cdot 10^{-2}$
τ_ρ graphene	157.58 ± 13.86	321.23 ± 83.51	$4.58 \cdot 10^{-2} \pm 1.70 \cdot 10^{-2}$

Times comparison

Different approaches can be found in the literature in order to measure bulk characteristic time.[S25–S31] On the one hand, the question of which characteristic time is the main contribution to viscosity temperature dependence remains open, i.e. whether the total decay time τ_ρ or only the long time behavior τ_α is needed. On the other hand, we can also wonder about the suitability of different approaches to measure the τ_α decay time. In this paper, we measured τ_α from Gallo et al. fit[S32] for the intermediate scattering function $F(q,t)$:

$$F(q,t) = [1 - A(q)]e^{-(t/\tau_s)^2} + A(q)e^{-(t/\tau_l)^\gamma}, \tag{10}$$

with $\tau_\alpha = \tau_l \Gamma(1/\gamma)/\gamma$ where $\Gamma(x)$ is Euler function. Because for high temperatures $\gamma = 1$, sometimes a simple exponential decay has been considered for the long time behavior (τ_α from $1/e$ approach in Fig. S18).[S25–S30] Nevertheless, a better agreement should be found with Eq. (10) by considering the weight $A(q)$ (τ_α from A/e approach in Fig. S18).

In Fig. S18 left one can see that, globally, viscosity exponential decay with temperature is captured by the characteristic time measured from the different approaches. Nevertheless, the approach $1/e$ fails as an approximation of the $F(q,t)$ fit while more similar results were obtained when computing τ_α from the A/e approach.

In Fig. S18 right we compared the different τ_α measurements with the characteristic time chosen to describe bulk dynamics in our paper: τ_ρ. One can see that the temperature behavior of τ_α is different than the one of τ_ρ for any of the different approaches chosen, even for τ_α from the full $F(q,t)$ fit, where the different behaviors are clearer in the supercooled regime.

$D_{q_\parallel}$ and D_0 comparison

In Fig. S19 we show the different temperature evolution for both diffusion coefficients. The collective diffusion coefficient $D_{q_\parallel}$ has been computed from the total density relaxation time
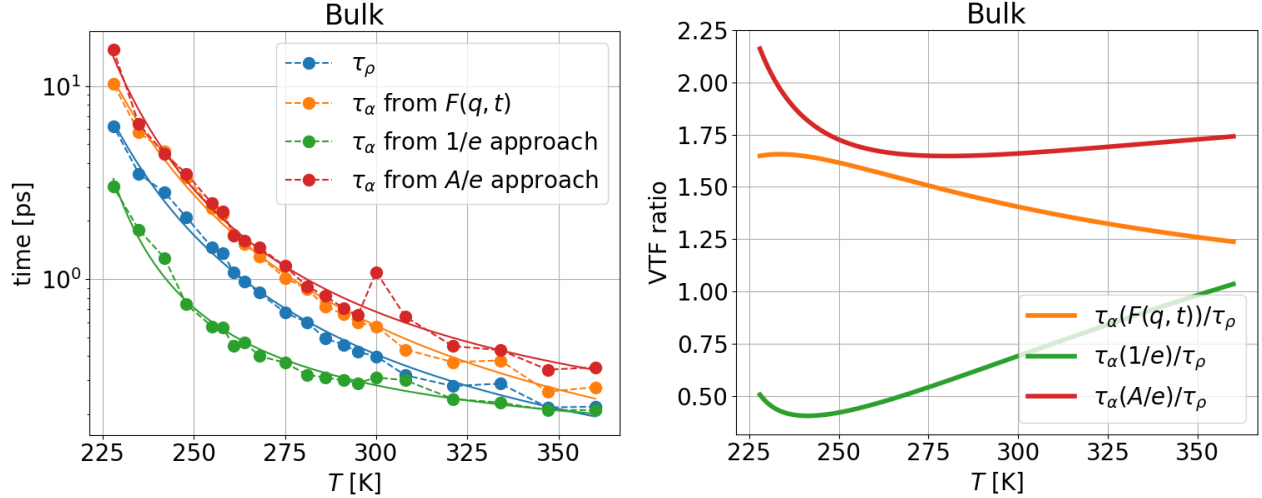
Figure S18: On the left, characteristic times measured from different approaches for bulk water as a function of temperature. In continuum line are represented their respective VTF fits. On the right, characteristic times VTF ratio with respect to the characteristic time considered in this work, τ_ρ, in order to highlight their different temperature dependence.

τ_ρ by the relation $D_{q_\parallel} = 1/(q_\parallel^2 \tau_\rho)$. The self-diffusion coefficient D_0 values are taken from.[S20] We can observe that both diffusion coefficients are of the same order of magnitude around room temperature, but their temperature evolution is quite different.

References

(S1) Plimpton, S. Fast parallel algorithms for short-range molecular dynamics. *Journal of computational physics* **1995**, *117*, 1–19.

(S2) Abascal, J. L.; Vega, C. A general purpose model for the condensed phases of water: TIP4P/2005. *The Journal of chemical physics* **2005**, *123*, 234505.

(S3) Huang, D. M.; Cottin-Bizonne, C.; Ybert, C.; Bocquet, L. Aqueous electrolytes near hydrophobic surfaces: Dynamic effects of ion specificity and hydrodynamic slip. *Langmuir* **2008**, *24*, 1442–1450.

(S4) Fu, L.; Joly, L.; Merabia, S. Giant Thermoelectric Response of Nanofluidic Systems Driven by Water Excess Enthalpy. *Physical Review Letters* **2019**, *123*, 138001.
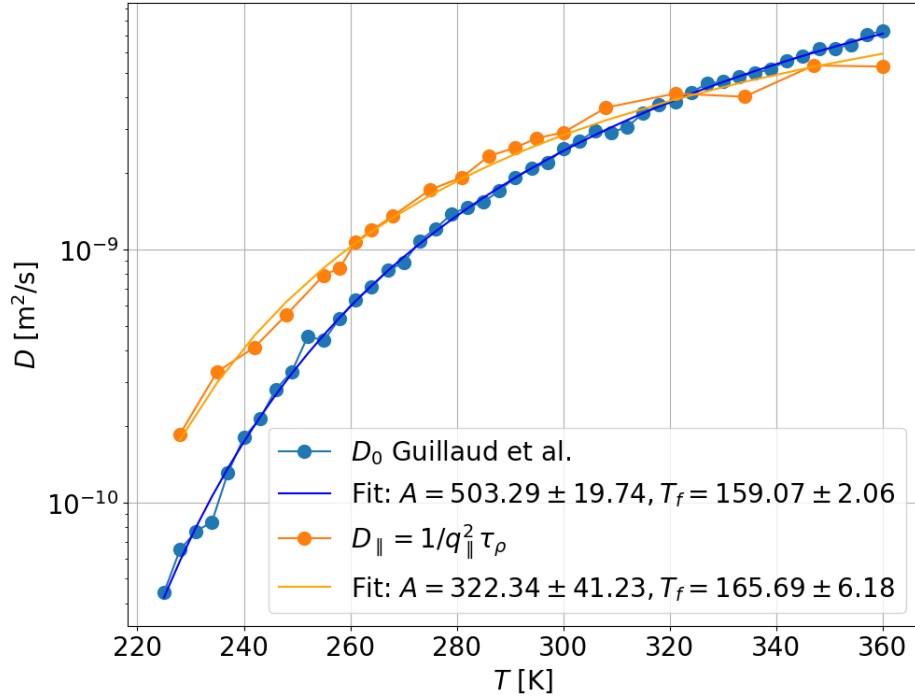
Figure S19: Self-diffusion coefficient D_0 from[S20] and collective diffusion coefficient $D_{q_\parallel}$ as a function of temperature. We can observe that both diffusion coefficients are on the same order of magnitude around room temperature, but their temperature evolutions are different. In continuum line it is represented the respective fits by an inverse VTF law.

(S5) Falk, K.; Sedlmeier, F.; Joly, L.; Netz, R. R.; Bocquet, L. Molecular origin of fast water transport in carbon nanotube membranes: superlubricity versus curvature dependent friction. *Nano letters* **2010**, *10*, 4067–4073.

(S6) Schnabel, T.; Srivastava, A.; Vrabec, J.; Hasse, H. Hydrogen bonding of methanol in supercritical CO2: comparison between 1H NMR spectroscopic data and molecular simulation results. *The Journal of Physical Chemistry B* **2007**, *111*, 9871–9878.

(S7) Guevara-Carrion, G.; Vrabec, J.; Hasse, H. Prediction of self-diffusion coefficient and shear viscosity of water and its binary mixtures with methanol and ethanol by molecular simulation. *The Journal of chemical physics* **2011**, *134*, 074508.

(S8) Herrero, C.; Omori, T.; Yamaguchi, Y.; Joly, L. Shear force measurement of the hydrodynamic wall position in molecular dynamics. *The Journal of chemical physics* **2019**, *151*, 041103.

(S9) Bocquet, L.; Barrat, J.-L. Flow boundary conditions from nano-to micro-scales. *Soft matter* **2007**, *3*, 685–693.

(S10) Debenedetti, P. G.; Stillinger, F. H. Supercooled liquids and the glass transition. *Nature* **2001**, *410*, 259–267.

(S11) Vogel, H. The law of the relation between the viscosity of liquids and the temperature. *Phys. Z* **1921**, *22*, 645–646.

(S12) Tammann, G.; Hesse, W. The dependence of viscosity upon the temperature of supercooled liquids. *Z. Anorg. Allg. Chem* **1926**, *156*, 245–257.

(S13) Fulcher, G. S. Analysis of recent measurements of the viscosity of glasses. *Journal of the American Ceramic Society* **1925**, *8*, 339–355.

(S14) Speedy, R.; Angell, C. Isothermal compressibility of supercooled water and evidence for a thermodynamic singularity at- 45 C. *The Journal of Chemical Physics* **1976**, *65*, 851–858.

(S15) Bässler, H. Viscous flow in supercooled liquids analyzed in terms of transport theory for random media with energetic disorder. *Physical review letters* **1987**, *58*, 767.

(S16) Shi, R.; Russo, J.; Tanaka, H. Common microscopic structural origin for water's thermodynamic and dynamic anomalies. *The Journal of Chemical Physics* **2018**, *149*, 224502.

(S17) Hallett, J. The temperature dependence of the viscosity of supercooled water. *Proceedings of the Physical Society* **1963**, *82*, 1046.

(S18) Dehaoui, A.; Issenmann, B.; Caupin, F. Viscosity of deeply supercooled water and its coupling to molecular diffusion. *Proceedings of the National Academy of Sciences* **2015**, *112*, 12020–12025.

(S19) Markesteijn, A. P.; Hartkamp, R.; Luding, S.; Westerweel, J. A comparison of the value of viscosity for several water models using Poiseuille flow in a nano-channel. *The Journal of Chemical Physics* **2012**, *136*, 134104.

(S20) Guillaud, E.; Merabia, S.; de Ligny, D.; Joly, L. Decoupling of viscosity and relaxation processes in supercooled water: a molecular dynamics study with the TIP4P/2005f model. *Physical Chemistry Chemical Physics* **2017**, *19*, 2124–2130.

(S21) Tocci, G.; Joly, L.; Michaelides, A. Friction of water on graphene and hexagonal boron nitride from ab initio methods: very different slippage despite very similar interface structures. *Nano letters* **2014**, *14*, 6872–6877.

(S22) Barrat, J.-L.; Bocquet, L. Influence of wetting properties on hydrodynamic boundary conditions at a fluid/solid interface. *Faraday Discuss.* **1999**, *112*, 119–128.

(S23) Govind Rajan, A.; Strano, M. S.; Blankschtein, D. Liquids with Lower Wettability Can Exhibit Higher Friction on Hexagonal Boron Nitride: The Intriguing Role of Solid–Liquid Electrostatic Interactions. *Nano letters* **2019**, *19*, 1539–1551.

(S24) Steele, W. A. The physical interaction of gases with crystalline solids: I. Gas-solid energies and properties of isolated adsorbed atoms. *Surface Science* **1973**, *36*, 317–352.

(S25) Yamamoto, R.; Onuki, A. Heterogeneous diffusion in highly supercooled liquids. *Physical review letters* **1998**, *81*, 4915.

(S26) Kumar, P.; Buldyrev, S. V.; Becker, S. R.; Poole, P. H.; Starr, F. W.; Stanley, H. E. Relation between the Widom line and the breakdown of the Stokes-Einstein relation in supercooled water. *Proceedings of the National Academy of Sciences* **2007**, *104*, 9575–9579.

(S27) Jeong, D.; Choi, M. Y.; Kim, H. J.; Jung, Y. Fragility, Stokes–Einstein violation, and correlated local excitations in a coarse-grained model of an ionic liquid. *Physical Chemistry Chemical Physics* **2010**, *12*, 2001.

(S28) Xu, L.; Mallamace, F.; Yan, Z.; Starr, F. W.; Buldyrev, S. V.; Stanley, H. E. Appearance of a fractional Stokes–Einstein relation in water and a structural interpretation of its onset. *Nature Physics* **2009**, *5*, 565–569.

(S29) Ikeda, A.; Miyazaki, K. Glass Transition of the Monodisperse Gaussian Core Model. *Physical Review Letters* **2011**, *106*, 015701.

(S30) Shi, Z.; Debenedetti, P. G.; Stillinger, F. H. Relaxation processes in liquids: Variations on a theme by Stokes and Einstein. *The Journal of chemical physics* **2013**, *138*, 12A526.

(S31) Kawasaki, T.; Kim, K. Identifying time scales for violation/preservation of Stokes-Einstein relation in supercooled water. *Science Advances* **2017**, *3*, e1700399.

(S32) Gallo, P.; Sciortino, F.; Tartaglia, P.; Chen, S.-H. Slow Dynamics of Water Molecules in Supercooled States. *Phys. Rev. Lett.* **1996**, *76*, 2730–2733.